

---

This is an electronic reprint of the original article.  
This reprint may differ from the original in pagination and typographic detail.

Baghdadi, R.; Arpaia, R.; Charpentier, S.; Golubev, D.; Bauch, T.; Lombardi, F.  
**Fabricating Nanogaps in YBa<sub>2</sub>Cu<sub>3</sub>O<sub>7-d</sub> for Hybrid Proximity-Based Josephson Junctions**

*Published in:*  
Physical Review Applied

*DOI:*  
[10.1103/PhysRevApplied.4.014022](https://doi.org/10.1103/PhysRevApplied.4.014022)

Published: 01/01/2015

*Document Version*  
Publisher's PDF, also known as Version of record

*Please cite the original version:*  
Baghdadi, R., Arpaia, R., Charpentier, S., Golubev, D., Bauch, T., & Lombardi, F. (2015). Fabricating Nanogaps in YBa<sub>2</sub>Cu<sub>3</sub>O<sub>7-d</sub> for Hybrid Proximity-Based Josephson Junctions. *Physical Review Applied*, 4(1), 014002.  
<https://doi.org/10.1103/PhysRevApplied.4.014022>

---

This material is protected by copyright and other intellectual property rights, and duplication or sale of all or part of any of the repository collections is not permitted, except that material may be duplicated by you for your research use or educational purposes in electronic or print form. You must obtain permission for any other use. Electronic or print copies may not be offered, whether for sale or otherwise to anyone who is not an authorised user.

# Fabricating Nanogaps in $\text{YBa}_2\text{Cu}_3\text{O}_{7-\delta}$ for Hybrid Proximity-Based Josephson Junctions

Reza Baghdadi,<sup>1</sup> Riccardo Arpaia,<sup>1</sup> Sophie Charpentier,<sup>1</sup> Dmitri Golubev,<sup>2,3</sup> Thilo Bauch,<sup>1</sup> and Floriana Lombardi<sup>1,\*</sup>

<sup>1</sup>*Quantum Device Physics Laboratory, Department of Microtechnology and Nanoscience, Chalmers University of Technology, 41296 Göteborg, Sweden*

<sup>2</sup>*Low Temperature Laboratory (OVLL), Aalto University School of Science, P.O. Box 13500, FI-00076 Aalto, Finland*

<sup>3</sup>*Institute of Nanotechnology, Karlsruhe Institute of Technology, D-76021 Karlsruhe, Germany*

(Received 8 April 2015; revised manuscript received 24 June 2015; published 29 July 2015)

The advances of nanotechnologies applied to high-critical-temperature superconductors (HTSs) have recently given a huge boost to the field, opening new perspectives for their integration in hybrid devices. The feasibility of this research goes through the realization of HTS nanogaps with superconductive properties close to the as-grown bulk material at the nanoscale. Here we present a fabrication approach allowing the realization of  $\text{YBa}_2\text{Cu}_3\text{O}_{7-\delta}$  (YBCO) nanogaps with dimensions as small as 35 nm. To assess the quality of the nanogaps, we measure, before and after an ozone treatment, the current-voltage characteristics and the resistance versus temperature of YBCO nanowires with various widths and lengths, fabricated by using different lithographic processes. The analysis of the superconducting transition with a thermally activated vortex-entry model allows us to determine the maximum damage the nanowires undergo during the patterning which relates to the upper bound for the dimension of the nanogap. We find that the effective width of the nanogap is of the order of 100 nm at the superconducting transition temperature while retaining the geometrical value of about 35 nm at lower temperatures. The feasibility of the nanogaps for hybrid Josephson devices is demonstrated by bridging them with thin Au films. We detect a Josephson coupling up to 85 K with an almost ideal magnetic-field response of the Josephson current. These results pave the way for the realization of complex hybrid devices, where tiny HTS nanogaps can be instrumental to study the Josephson effect through barriers such as topological insulators or graphene.

DOI: 10.1103/PhysRevApplied.4.014022

## I. INTRODUCTION

In recent years, the advances of nanotechnologies applied to high-critical-temperature superconductors (HTSs) have been such that the long-sought integration with semiconductor films or nanowires, organic electronic materials, and, more recently, materials characterized by a Dirac dispersion relation is slowly becoming a reality. Hybrid devices involving interfaces between HTSs and, for example, topological insulators (TIs) or graphene are extremely promising to reveal the new physics due to the proximity of a superconductor and a two-dimensional material with a Dirac cone [1–3]. There are several theoretical reports, which refer to the  $d$ -wave symmetry of the order parameter in HTSs and to the large value of the superconducting gap, to design experiments to stabilize and reveal the existence of Majorana fermions, still elusive particles in solid-state systems, that are supposed to nucleate at the interface between a superconductor and a TI [4–8]. Superconducting hybrid structures are also considered a crucial step towards a topological quantum computer, which would be exceptionally well protected

from errors, thanks to the non-Abelian statistics of Majorana fermions [9,10].

At the same time, by interfacing HTS nanogaps with graphene, one could get access to the quantum Hall effect in a regime of Josephson transport, made possible by the extremely high upper critical field of the HTS (of the order of 100 T) and superconducting gap. Fascinating physics aspects are expected to emerge from the transport of coherent Cooper pairs through opposite edge states in the quantum Hall regime. In particular, here Cooper pair transport could also play an important role in stabilizing even further the already robust quantum Hall plateaus in graphene [11–13].

The realization of HTS hybrid devices requires the engineering of reproducible and stable nanogaps, which is a challenging task because of the surface and chemical instability of thin films. In this paper, we present an approach that allows obtaining  $\text{YBa}_2\text{Cu}_3\text{O}_{7-\delta}$  (YBCO) planar nanogaps below 40 nm. This has been achieved by protecting the sides of the electrodes with a Pt/Au bilayer during subsequent  $e$ -beam lithography steps and by using a soft (low-temperature) resist baking. In future hybrid devices, the superconducting proximity will then be induced through the noble metal layer that has to be thin enough to take advantage of the large HTS

\*floriana.lombardi@chalmers.se

superconducting gap. The aim of this work is twofold: (a) to get proper estimates for the effective size of the HTS nanogaps, representing the ultimate channel length in hybrid structures, and (b) to show the feasibility of the YBCO nanogaps to induce a proximity Josephson coupling when bridged with a conventional normal metal [14]. This is a crucial step for interfacing with more complex materials. In particular, we show that the Au/YBCO interface involved in the Josephson tunneling is close to the optimal doped regime, which is of high relevance to achieve high Josephson current values.

Previous attempts to realize superconductor–normal-metal–superconductor ( $S$ - $N$ - $S$ ) junctions with YBCO nanogaps used the possibility of breaking the continuity of YBCO films when grown on trenches or steps fabricated in the substrate. In pioneering works, trenches with a high aspect ratio are patterned by using  $\text{Ar}^+$  ion milling [15] or focused-ion-beam milling (FIB) [16]. The YBCO film subsequently deposited is found, in certain conditions, to break across the trenches. An alternative way explores the use of a step patterned in the substrate: by depositing YBCO under an angle, the shadowing effect of the step could induce the growth of a discontinuous film across the step itself [17,18]. In other reports, the discontinuity of the YBCO is achieved after the deposition of a MgO layer kept only in the region of the step [19,20]. However, these approaches suffer from the random formation of YBCO grain boundaries at the edges of the trenches or steps. They would act as weak links, mimicking the Josephson behavior of the final  $S$ - $N$ - $S$  structure. These techniques rely on the deposition of an *in situ* Au/Ag film, acting as a normal barrier to realize the  $S$ - $N$ - $S$  junction, in order to minimize the contact resistance between the YBCO and the normal metal. Furthermore, these approaches seem to be incompatible for interfacing of YBCO electrodes with materials other than Au/Ag such as TIs, graphene, or even organic conductors. Attempts to obtain planar YBCO nanogaps, by a direct patterning of YBCO with FIB [21,22] or  $\text{Ar}^+$  ion milling [23], followed by a deposition of a normal metal to realize  $S$ - $N$ - $S$  junctions, do not have follow-up results. But, more importantly, the poor reproducibility of the various techniques remains an unresolved issue.

Here we show that highly reproducible planar YBCO nanogaps can be obtained by the complete Au “encapsulation” of the electrodes, forming the nanogap. This is essential to limit the extension of the damaged area on the inner sides of the YBCO nanogap, minimizing the effective length of the nanochannel. In general, to interface YBCO nanogaps with graphene, TI flakes, or nanowires, two  $e$ -beam lithography (EBL) steps would, in principle, be sufficient to define hybrid nanostructure: the first EBL to pattern YBCO nanogaps, and the second one to contact the flakes or nanowires once they have been transferred on the substrate. However, since YBCO easily degrades by getting

in contact with chemicals such as  $e$ -beam resists, the second lithography steps would seriously enlarge the effective width of the nanogap, making the observation of the superconducting proximity effect very critical. For YBCO hybrid devices, before the transferring of the flake or nanowire, the sides of patterned YBCO need to be protected with a noble-metal layer. This implies further extremely challenging  $e$ -beam lithography for reopening the nanogap by removing the new Au layer deposited across it.

To assess the extension of the damaged regions of the YBCO electrodes and therefore the effective length of the channel, we focus on the study of the superconducting transport properties of a “prototype” for the realization of HTS nanogaps: a YBCO nanowire capped with a thin Au layer (20 nm).

The main idea is to study the regime of fluctuations in superconducting nanowires (with the top and sides covered by a Pt/Au bilayer in analogy with the nanogaps), which undergoes the same processing steps as the ultimate YBCO nanogaps. From the analysis of the resistance versus temperature  $R(T)$  data, we can extract the upper limit for the damaged regions, which is discussed in more detail further on in the text. This is also fundamental to understand the Josephson properties of the junctions obtained by bridging the nanogap with a normal metal.

## II. DEVICE FABRICATION

For the realization of the devices, a 50-nm-thick YBCO film is deposited on a MgO (1 1 0) substrate, suitable for high-frequency characterization [24], using pulsed laser deposition (PLD). The deposition conditions (e.g., substrate temperature, background oxygen pressure, laser energy, and cooling-down rate) are optimized to achieve high-quality, epitaxial  $c$ -axis-oriented YBCO films with a smooth surface with roughness less than 1.5 nm. All YBCO films exhibit a critical temperature ( $T_c$ ) between 85 and 86 K with a 1-K-wide resistive transition. Structural characterization [25] allows us to establish that the starting films are in the overdoped region of the superconducting dome. The YBCO film is then *in situ* covered with a 20-nm-thick Au film. Then, a 70-nm-thick layer of diamondlike carbon (DLC), acting as a hard mask during the ion milling of the YBCO nanogap, is deposited by PLD [26]. Because of its extremely low  $\text{Ar}^+$  etching rate, the thin layer of DLC film is an excellent masking material for realizing sub-100-nm features [27].

The fabrication process is schematically depicted in Figs. 1(a)–1(h). It involves three EBL steps. First, we fabricate the nanowires and the current probes by following the procedure described in Refs. [26,28] [whose result is schematically illustrated in Fig. 1(a)]. Then, a bilayer of Pt (10 nm)/Au (50 nm) is deposited on the entire chip including the side walls of YBCO structures [Fig. 1(b)]. A second EBL procedure is used to finalize the

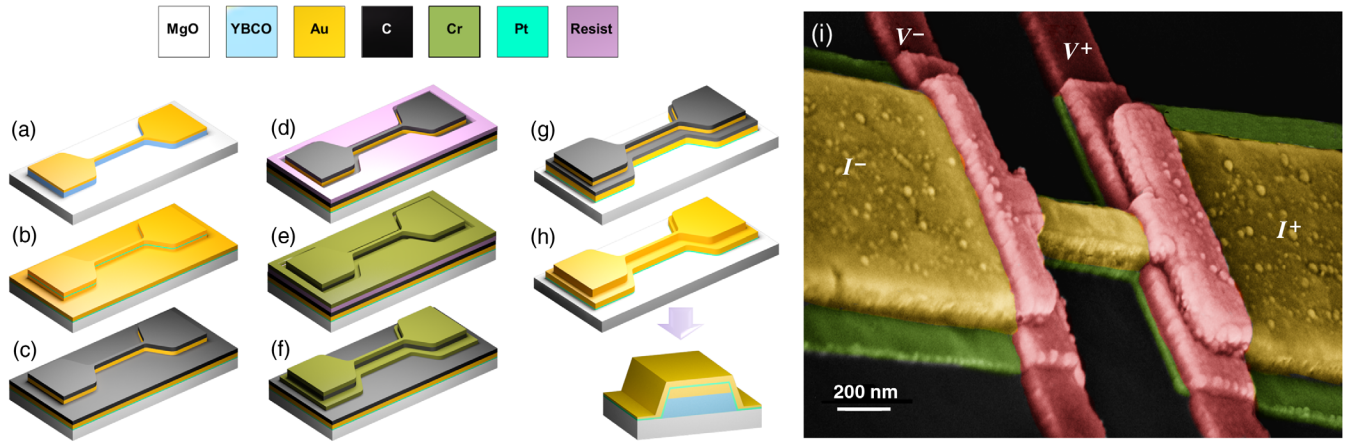


FIG. 1. Fabrication flow to cover the edges of the nanowire with a Pt/Au bilayer: (a) freestanding YBCO nanowire capped with Au as fabricated with 1EBL; (b) the entire sample is covered by a sputter-deposited bilayer of Pt/Au; (c) a DLC film serving as a hard etching mask is deposited by PLD; (d) a single-layer, diluted resist (ZEP 520A: Anisole) is spun, exposed, and developed; (e) a Cr layer is evaporated on the entire device; (f) the mask is defined after Cr is lifted off; (g) after removing the uncovered DLC by oxygen plasma etching, a gentle  $\text{Ar}^+$  ion milling is used to define the encapsulated nanowire, etching the Pt/Au film from the substrate regions; (h) the residual DLC film on top of the nanostructure is removed in oxygen plasma. The inset shows the corresponding cross section of the device. Here it is worth mentioning that the final shape of the nanowire is trapezoidal: the width  $w$  of the nanowire is defined as the width at half thickness, corresponding to the mean value between the top width  $w_t$  and the bottom width  $w_b$ , determined from atomic force microscopy (AFM) and scanning electron microscopy (SEM) analysis [29]. (i) SEM picture of the final 3EBL device. Here the protective Pt/Au double layer is represented in yellow and green, depending on whether it covers the top (yellow) or the sides (green) of the YBCO nanostructures. The Pt/Au electrodes defined by the lift-off technique as the last step of the nanopatterning procedure are highlighted in red.

encapsulation of the nanostructures [Figs. 1(c)–1(h)]. The transferred pattern is slightly larger (30–50 nm) with respect to the already-patterned nanowire layout. This is done to ensure that all the YBCO edges remain protected by Pt/Au after the ion milling of the Au [Fig. 1(h)]. Also in this case DLC is used as an etching mask. The third and last EBL step is performed to define the narrow voltage probes. With this type of electrode configuration, the temperature dependence of the resistive transition involves only the narrow nanowire and not the transition of the wide electrodes. A SEM image of the typical 3EBL device is shown in Fig. 1(i).

For comparison, we also fabricate YBCO nanowires covered with a thin Au film with a single and two EBL steps. In the first case, nanowires capped with Au are used as reference systems concerning the best superconductive properties one can achieve in a YBCO nanostructure under specific oxygen-doping conditions. They are referred to as 1EBL devices throughout this paper. In the latter case, instead the two lithography steps refer to the patterning of the nanowire capped with Au and to another processing for connecting the nanowire to the outer bonding pads by a lift-off procedure. In this case, the edges of the nanowire are unprotected and in direct contact with the resist and other chemicals during the second lithography step. These nanostructures are addressed as 2EBL devices. More details about the fabrication of 2EBL devices can be found in Supplemental Material [30].

### III. TRANSPORT PROPERTIES OF NANOWIRES PATTERNED WITH DIFFERENT PROCEDURES

#### A. Study of the critical current $J_C$ as a function of the nanowire width and length

We systematically study the transport properties of YBCO nanowires as a function of widths and lengths in the range of 60–700 nm and 1–10  $\mu\text{m}$ , respectively, for 1EBL, 2EBL, and 3EBL devices. The measurements are performed in a  $^3\text{He}$  cryostat with a base temperature of 300 mK. The current-voltage characteristics (IVCs) are measured by sweeping the current and measuring the voltage across the wire. The critical current density  $J_C$  for all devices is extracted and plotted in Fig. 2. The maximum critical current density of  $6.1 \times 10^7 \text{ A/cm}^2$  is achieved for a 200-nm-wide and 1- $\mu\text{m}$ -long nanowire processed with one EBL step (Fig. 2, red circles). Compared to our recent study [29], we do not observe the highest  $J_C$  for the narrowest wire. This is a consequence of the very thin Au (20 nm) capping layer we use for protection. In our previous report [29], we have shown that 50 nm is the minimum thickness of the Au capping required to preserve the pristine superconducting properties of the nanostructures. As also reported in other works, the decrease of the  $J_C$  for width below 200 nm could result from a partial degradation of YBCO nanostructure during the patterning [31–33]. Our choice to minimize the thickness of the Au layer is dictated by the final goal to realize superconducting hybrid devices. Since in these structures



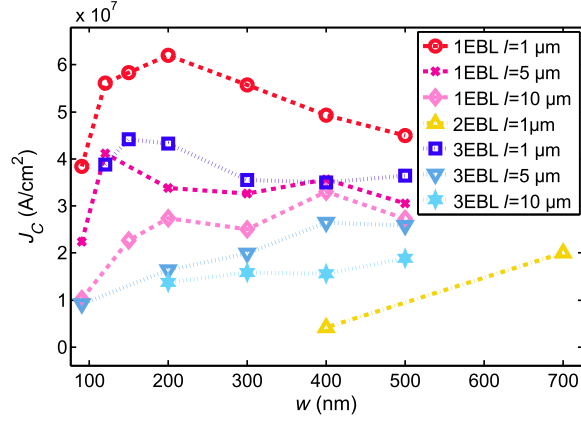


FIG. 2. Critical current density  $J_C$  versus width  $w$  for 1EBL, 2EBL, and 3EBL nanowires with different lengths.

the proximity will be induced through the Au layer, thinner thicknesses are able to warrant a stronger superconducting proximity. For the 1EBL samples, the decrease of  $J_C$  by increasing the nanowire width (above 200 nm) can be ascribed to current crowding effects [28]. It is also evident that for 1EBL the maximum  $J_C$  value is reduced for a longer length of nanowires (dark red crosses, pink diamonds) and is almost independent of the nanostructure width above 200 nm. At such extended lengths, it is possible that inhomogeneities in the film, rather than current crowding, have a major effect on the value of  $J_C$ . This would naturally explain the almost-constant value of  $J_C$  as a function of the width for the longest nanowires. Below 200-nm width, also in these cases the  $J_C$  decreases by reducing the width as a result of degradation of the superconducting properties at the smallest width. It is worth mentioning that all the data for 1EBL refer to nanowires patterned on the same chip and that therefore are not influenced by the possible random variations due to film quality or nanopatterning procedure that can affect nanostructures fabricated on different chips.

The same  $J_C$  trend is also observed for 3EBL devices (see Fig. 2: blue squares, light blue triangles, and cyan stars). In this case, the maximum value of  $4.5 \times 10^7$  A/cm<sup>2</sup> is achieved for a 150-nm-wide and 1- $\mu$ m-long nanowire and is only about 20% lower than the values obtained for 1EBL. This confirms that the superconducting properties of the YBCO nanowires are well preserved even though the nanostructure is undergoing several lithographic procedures.

In contrast to 1EBL and 3EBL, the 2EBL devices show a significant reduction in the  $J_C$  values for nanowires with the shortest length (1  $\mu$ m). The fact that we observe such a huge reduction of the  $J_C$  is that the resist and chemicals, in general, are in direct contact with the YBCO edges of the patterned nanowire during the fabrication, which has an adverse effect on the superconducting properties of the nanostructure. Moreover, the 2EBL devices do not show

any superconducting transition for the widths below 400 nm. This means that the damaged nonsuperconducting region extends approximately for about 200 nm from both lateral sides of the nanowire. YBCO nanogaps, fabricated by using a 2EBL procedure, would have an effective width 400 nm larger than the geometrical-nominal one, which would make the observation of proximity-induced superconductivity very hard to detect [34].

## B. Analysis of the resistance versus temperature transition

As a further characterization of the nanowires fabricated with different procedures, we measure the resistance versus temperature  $R(T)$  of 1EBL and 3EBL devices. Figure 3 shows the superconducting transition of both 1EBL and 3EBL devices of comparable widths. The curves are characterized by a broadening, which is larger in 3EBL devices. Such a broadening, expected in nanowires with width  $w$  much larger than the coherence length  $\xi$  [ $w \gg 4.4\xi(T)$  even at  $T \approx T_C$ ], can be ascribed to the dissipation induced by vortices, perpendicular to the bias current, crossing the nanowire [35–38]. The resistance of 1EBL and 3EBL nanowires can be written as

$$R(T) = [R_v^{-1}(T) + R_{sh}^{-1}]^{-1}, \quad (1)$$

where  $R_{sh}$  is the shunt resistance associated with the gold layer, corresponding to the resistance value measured at the onset of the superconducting transition, and  $R_v$  is the thermally activated vortex-entry resistance, which can be expressed as

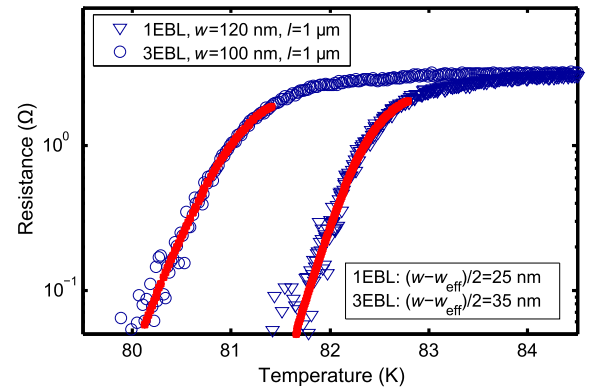


FIG. 3. Resistance versus temperature of a 1EBL nanowire (triangles) and of a 3EBL nanowire (circles), having the same length and similar width. The lines are the fits to the two data sets, using a thermally activated vortex-entry model. As a consequence of local inhomogeneities introduced by the nanopatterning procedure and of the oxygen out-diffusion, we have to consider a discrepancy between the geometrical and effective widths, of 25 and 35 nm per edge for 1EBL and 3EBL devices, respectively. This allows a good fit of the data using the typical values of  $\lambda_0$  and  $\xi_0$  for YBCO thin films and the same  $T_C$  for both wires.

$$R_v(T) = 7.1R_{\square} \frac{4l\xi(T)}{(w_b + w_t)^2} \left( \frac{\epsilon_0(T)}{k_B T} \right)^{3/2} \exp \left( -\frac{U_{\max}(T)}{k_B T} \right), \quad (2)$$

with

$$U_{\max}(T) = \epsilon_0(T) \left( \frac{w_b \ln \frac{1.47w_b}{\pi\xi(T)} - w_t \ln \frac{1.47w_t}{\pi\xi(T)}}{w_b - w_t} - 1 \right). \quad (3)$$

In Eqs. (2) and (3),  $R_{\square}$  and  $l$  are, respectively, the sheet resistance and the length of the wire,  $k_B$  is the Boltzmann constant, and  $\epsilon_0(T) = \Phi_0^2 t / 4\pi\mu_0\lambda_L^2(T)$  is the characteristic energy of a vortex in thin films, with  $\Phi_0 = h/2e$  the superconducting flux quantum and  $\mu_0$  the vacuum permeability. The temperature dependence of the London penetration depth and of the coherence length are given by [37]  $\lambda_L(T) = \lambda_0[1 - (T/T_C)^2]^{-1/2}$  and  $\xi(T) = \xi_0[1 - (T/T_C)^2]^{-1/2}$ , where  $\lambda_0$  and  $\xi_0$  represent the zero-temperature values. Equations (2) and (3) refine the expression we have previously considered in Refs. [25,37], since it takes into consideration that the cross section of our nanowires is trapezoidal (hence the top width  $w_t$  differs from the bottom width  $w_b$ ).

According to Eq. (2), the superconducting transition becomes broader when decreasing the wire width  $w$  and thickness  $t$ . In previous reports [37,39], we show that in YBCO nanowires protected by a 50-nm-thick Au layer the broadening at the transition can be fitted with Eqs. (1) and (2) considering the geometrical nanowire dimensions. The extracted values for  $\lambda_0$  (approximately 270 nm) and  $\xi_0$  (approximately 2.5 nm) are typical for YBCO thin films [40,41]. For the devices shown in Fig. 3, as a consequence of the very thin capping Au layer used in this work, the superconducting transition can be still very well fitted with Eq. (1) but only by assuming for the 1EBL nanowires approximately 25 nm of damage on both lateral sides, i.e., an effective width  $w_{\text{eff}}$  smaller than the geometrical one.

This is obtained while keeping the typical values for  $\lambda_0$  (approximately 270 nm) and  $\xi_0$  (approximately 2.5 nm).

The 3EBL devices have instead a larger broadening compared to 1EBL nanowires even for equal cross sections. Such broadening can again be nicely fitted by means of Eqs. (1) and (2), using a slightly larger damage of about 35 nm for each side (also in this case fixing  $\lambda_0 = 270$  nm and  $\xi_0 = 2.5$  nm). Such a variation with respect to 1EBL “reference” devices can be explained by considering that local inhomogeneities and oxygen out-diffusion become more relevant as a consequence of multiple lithographic procedures.

Here it is worth pointing out that the  $w_{\text{eff}}$  we extract from the  $R(T)$  fitting should be considered as a measure of the uniformity of the superconductive properties within 1–2 K from the critical-temperature onset. More specifically, the “damaged” area is caused by nonstoichiometric or oxygen-depleted paths, with a possible weakened superconductivity (and therefore a lower  $T_C$  onset below the one of the observed superconducting transition), that do not contribute to the fluctuation regime determining the broadening of the  $R(T)$  transition. However, we believe that these paths contribute instead to the superconducting transport properties of the nanowire at lower temperatures even though with a possible reduced critical current density. To verify if this scenario is possible in our nanostructures, we calculate the critical current densities  $J_C^{\text{eff}}$  one would get from the measured critical currents and assuming the effective width  $w_{\text{eff}}$  extracted from the  $R(T)$  fitting. The values of  $J_C^{\text{eff}}$  at 300 mK are reported for several wires fabricated with 1EBL and 3EBL nanowires (see Table I). These values are about 50% larger than the theoretical depairing limit value  $J_{\text{dep}}^{\text{GL}} \approx 6 \times 10^7$  A/cm<sup>2</sup> one would get within the Ginzburg-Landau theory in the low-temperature limit (assuming  $\lambda_0 \approx 270$  nm and  $\xi_0 \approx 2.5$  nm) [42]. If the  $J_C$  is limited by vortex entry, the maximum value a nanowire with  $w \gg 4.4\xi$  can carry is predicted to be very close to  $J_{\text{dep}}^{\text{GL}}$  [36]. Whatever mechanism is determining the maximum  $J_C$ , we conclude that the  $w_{\text{eff}}$  at 300 mK has to be

TABLE I. The critical current densities  $J_C$  of the narrowest 1- $\mu\text{m}$ -long 1EBL and 3EBL nanowires, measured at 300 mK and presented in Fig. 2, are compared to the effective critical current densities  $J_C^{\text{eff}}$ , calculated by using the  $w_{\text{eff}}$  extracted as a fit parameter from the superconducting transition (in 1EBL devices,  $w_{\text{eff}} = w - 50$  nm; in 3EBL devices,  $w_{\text{eff}} = w - 70$  nm). These  $J_C^{\text{eff}}$  values are higher than the expected depairing critical current limit, that in the Ginzburg-Landau theory is written as  $J_{\text{dep}}^{\text{GL}}(T) = \Phi_0[3^{3/2}\pi\mu_0\lambda^2(T)\xi(T)]^{-1}$  and whose value is  $6 \times 10^7$  A/cm<sup>2</sup> in the limit of low temperature, assuming  $\lambda_0 \approx 270$  nm and  $\xi_0 \approx 2.5$  nm.

Device	$J_C = I_C/(wt)$ (A/cm <sup>2</sup> )	$J_C^{\text{eff}} = I_C/(w_{\text{eff}}t)$ (A/cm <sup>2</sup> )
1EBL $w = 90$ nm	$3.84 \times 10^7$	$8.64 \times 10^7$
1EBL $w = 120$ nm	$5.62 \times 10^7$	$9.63 \times 10^7$
1EBL $w = 150$ nm	$5.84 \times 10^7$	$8.76 \times 10^7$
1EBL $w = 200$ nm	$6.20 \times 10^7$	$8.27 \times 10^7$
3EBL $w = 120$ nm	$3.88 \times 10^7$	$9.31 \times 10^7$
3EBL $w = 150$ nm	$4.41 \times 10^7$	$8.27 \times 10^7$
3EBL $w = 200$ nm	$4.32 \times 10^7$	$6.65 \times 10^7$

substantially larger than the value extracted close to  $T \approx T_C$ , and therefore the damaged regions on the side of the wires do contribute to the superconducting transport at lower temperatures.

### C. Comparison of the nanowire transport properties before and after ozonation

To assess the relevance of oxygen out-diffusion during the nanopatterning of YBCO films, the ion milling, and the resist baking and to possibly “cure” our devices by proper reoxygenation, we develop an *ex situ* ozone treatment [25]. The ozone treatment has been already intensively used for decades in order to improve the superconducting properties of YBCO thin films and nanostructures [43,44]. In our case, the samples are placed in a chamber at atmospheric pressure, in which ozone is produced by the absorption in oxygen atoms of 185 and 254 nm ultraviolet light. In such an environment, the samples are kept for 2 h at 150 °C and then slowly cooled down.

We study the effect of the ozone on 1EBL nanowires, as a function of both the wire width and length. Figure 4 summarizes the main results. For the 1- $\mu\text{m}$ -long nanowires, characterized by very high critical current densities (though lower than the depairing limit for narrowest widths), a  $J_C$  enhancement in the range 15%–20% is clearly visible for all the widths [see Fig. 4(a), which shows data of nanowires all realized on the same chip before and after ozone treatment]. As a consequence of the ozone annealing, the YBCO nanowires improve their superconducting properties, reaching  $J_C$  values very close to the depairing limit [28,29] or higher [45]. As a further confirmation of the high degree of homogeneity acquired by the nanowires after the ozonation, we have also shown in Ref. [25] that the superconducting transition of the ozonized nanowires is characterized by a smaller broadening, which can be fitted by means of Eqs. (1) and (2) without assuming any damage

on the sides. However, the effect of ozone becomes much more prominent in the longest nanowires. For these devices, presenting a substantial reduction of the  $J_C$ , as shown in Fig. 2 (pink diamonds), the increase of critical current after the ozonation can be up to 200%, as shown in Fig. 4(b). The validity of this treatment in supplying oxygen to the nanostructure, out-diffused during the nanopatterning procedure, is confirmed by the reduction of the critical temperature  $T_C$  after ozonation [see the inset in Fig. 4(b)], which is strictly related to a variation of the oxygen doping inside the nanostructures toward the over-doped region of the YBCO phase diagram [25]. Moreover, in very long and narrow 1EBL nanowires, the superconducting transition is not only quite broad, but it also presents a bump, which is a clear footprint of deoxygenated regions, with a lower critical temperature, having the size of the entire wire cross section [see the inset in Fig. 4(b)]. In such cases, the ozonation procedure makes the transition narrower, dissolving the bump and making the nanostructure more homogeneous.

The 3EBL nanowires could, in principle, benefit in the same way from the ozone annealing. However, the ozonation can act differently depending on whether it is performed after the first or the third lithographic step. As we show in a previous work [25], the oxygen refilling obtained with the ozonation mainly occurs through the lateral sides of the nanowires, since the oxygen mobility is much higher in the  $a$ - $b$  planes than along the  $c$ -axis direction [44,48]. To observe in 3EBL nanowires the same effect observed in very long 1EBL ones [see Fig. 4(b)], the ozonation has to be performed after the first lithographic step, before the wire is encapsulated by the Pt/Au layer, since the protecting layer acts as a barrier for the oxygen to diffuse into the YBCO.

Here we discuss the consequence of the ozonation on already-encapsulated nanowires (3EBL). For such

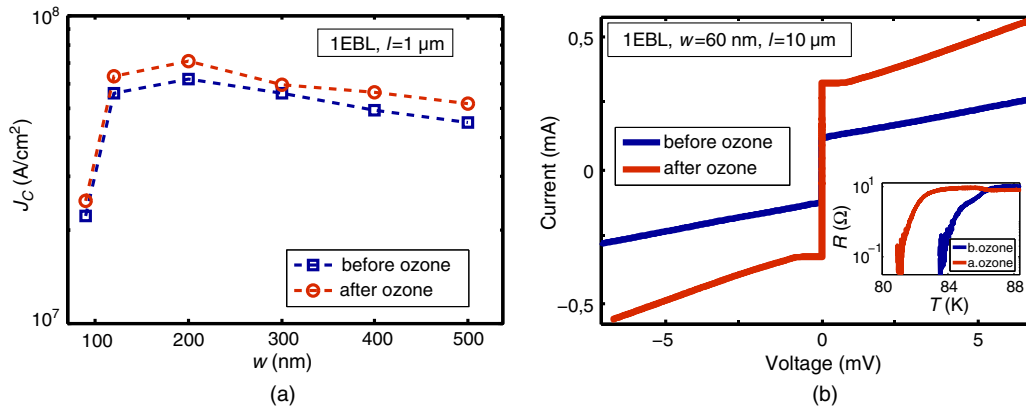


FIG. 4. (a) Critical current densities  $J_C$  of 1- $\mu\text{m}$ -long 1EBL nanowires, measured before and after the ozone treatment, as a function of the wire width. As a consequence of the ozone treatment, a  $J_C$  enhancement in the range 15%–20% is clearly visible for all the widths. (b) Current voltage characteristic of a 60-nm-wide and 10- $\mu\text{m}$ -long 1EBL nanowire before and after ozone treatment. In the inset, the resistive transition of the same nanowire before and after ozonation is shown. The critical temperature decreases by more than 2.5 K as a consequence of the ozone treatment.

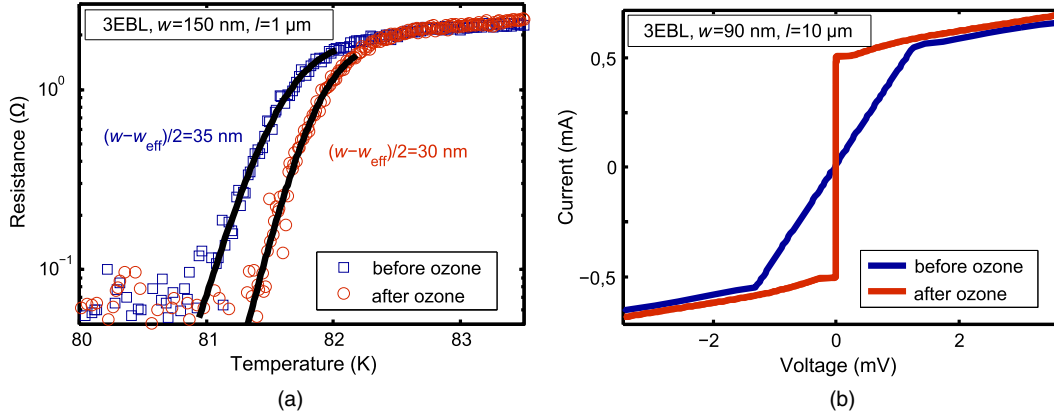


FIG. 5. (a) Resistance versus temperature of a 3EBL nanowire before and after the ozone treatment. Differently from the 1EBL nanowires, the main effect is an increase of the critical temperature. In addition, a reduction of 0.2 K in the transition broadening is visible: as a consequence, the data after ozonation can be fitted with the vortex-entry model, assuming a reduced damage of the nanostructure on the sides with respect to that we can estimate before the ozone annealing (the black lines represent the two fits to the data). (b)  $IV$  characteristic measured before and after the ozone treatment on a 90-nm-wide, 10- $\mu\text{m}$ -long 3EBL nanowire: as a consequence of the ozonation, the wire, which was previously resistive, becomes superconducting. Hence, in 3EBL devices, the role of ozone is not to reoxygenate the structures but to redistribute the oxygen, healing the YBCO that was damaged by the nanopatterning procedure.

structures we observe a critical-temperature increase [Fig. 5(a)]. This can be simply explained by the fact that the encapsulation acts as a block for the oxygen, preventing it from entering into the nanostructure. At the same time, the broadening of the superconducting transition is slightly reduced, and it can be well fitted by considering the vortex-entry model and a damage region reduced by 5–10 nm for each of the edges of the nanowire compared to the situation before the ozonation [black lines in Fig. 5(a)]. To clarify the physical scenario, we study the IVCs of the 3EBL nanowires before and after ozonation. While the treatment does not increase the value of the critical current (in some cases the  $J_C$  is slightly reduced), it homogenizes the oxygen content within the encapsulated nanowire. As shown in Fig. 5(b) for a 90-nm-wide and 10- $\mu\text{m}$ -long nanowire, the IVC before the ozone treatment exhibits a residual resistance possibly due to oxygen deficiency and/or disorder, causing the YBCO to lose the superconductivity in a specific region (of the dimensions of the cross section) of the nanowire. After the annealing, the IVC of the nanowire shows instead a well-defined critical current density. Hence, we conclude that, even though the ozonation does not change the oxygen content of the YBCO nanowire, it homogenizes its stoichiometry, redistributing the oxygen atoms and healing regions where the superconductivity is absent. This picture is supported by the slight increase of  $T_C$  signifying a lower global oxygen doping due to the redistribution of oxygen atoms in the damaged regions and the consequent reduction of  $J_C$ . This demonstrates that encapsulated nanowires, which already show excellent superconducting properties as fabricated, can be further optimized by means of the ultraviolet light or ozone treatment. Depending on when the annealing is

performed, we can even tune the parameters such as the critical current density and the critical temperature, according to the requirements of the different experiments in which these structures will be employed.

#### IV. TRANSPORT THROUGH YBCO/AU INTERFACES

To study the electrical properties of our YBCO/AU interfaces, we realize a set of YBCO nanowires connected by one Au bar [see Figs. 6(a) and 6(b)]. The Au is removed from the top of the nanowires to get a well-defined contact geometry. From the point of view of the transport properties, the Au/YBCO interface is representative of those present in the nanogap. A typical conductance measurement as a function of the bias voltage is shown in Fig. 6(c) before and after ozonation. We clearly observe a tunnel-like conductance curve, after the ozonation, with the clear appearance of a gap structure at  $V \sim 50$  mV which is twice the value of the YBCO gap at the optimally doped regime. Here it is worth mentioning that the layout of the devices is such that we always measure two interfaces in series, which explains the doubling of the gap value in the conductance curve. Before the ozonation, instead, the curve has an anomalous voltage dependence [blue line in Fig. 6(c)] which could be fitted with  $V^\alpha$  with  $\alpha = 0.5$  in the low-bias regime [dotted yellow curve in Fig. 6(c)]. This kind of dependence has been previously observed in amorphous  $\text{Ge}_{1-x}\text{Au}_x$  films [49] and attributed to the modification of the density of states of the compound in proximity of the metal-insulator transition. In our case, the total conductance is the contribution from both the top and side contact. In particular, the side interface undergoes an oxygen loss



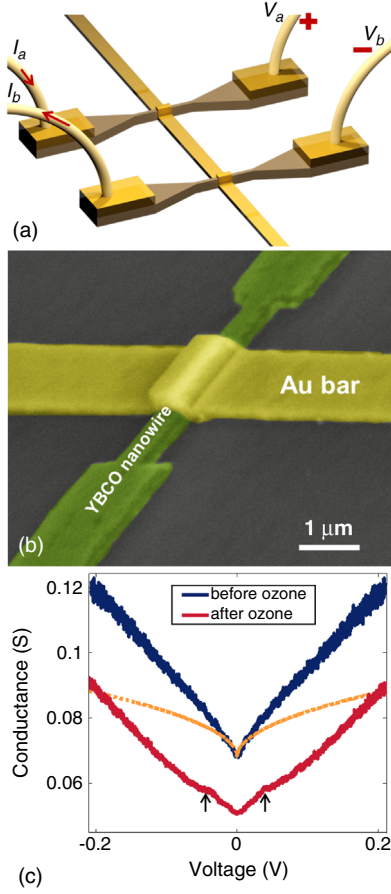


FIG. 6. (a) Schematic geometry of the YBCO/Au interfaces, with the YBCO nanowires connected by a Au bar. (b) SEM picture of the interface between the Au bar and one of the YBCO nanowires. (c) Conductance as a function of the voltage, before (blue) and after (red) the ozonation (the contribution of the Au bar is subtracted in both cases). The dashed line is the fit of the data before ozone, in the low-bias regime, with the expression  $I \propto bV^{1/2}$  [49].

during the patterning of the nanowire which leads to a YBCO layer at the interface with strongly degraded superconducting properties possibly close to the metal-insulator transition. After the ozonation, the disappearance of the

low-bias conductance anomaly and the occurrence of a gap feature in the conductance curve give a strong indication of a restored YBCO at the side interface. From the low-bias conductance values, we can estimate an average value for the contact resistivity of the YBCO/Au interface, from the top and side contact, of approximately  $4 \times 10^{-8} \Omega \text{ cm}^2$ . This value is among the best reported in the literature [15,16,50], corroborating the potentiality of the nanogap for proximity hybrid devices, that we demonstrate in the next paragraph.

## V. JOSEPHSON EFFECT THROUGH ENCAPSULATED NANOGAPS

Figure 7(a) shows an array of YBCO nanogaps fabricated by using a 3EBL procedure. Here the second lithography is used to remove the Pt/Au from the nanogaps while preserving the bilayer on the edge of the electrodes. The picture clearly shows well-defined nanogaps over several micron distances with a width below 40 nm. By considering that the maximum damage occurring to the electrodes is of the order of 30 nm (after the ozonation) close to  $T_C$ , the effective size of the nanogap is at most 100 nm at the transition temperature of the YBCO. At lower temperatures, instead we can expect that the extension of the nanogap is very close to 35 nm.

To probe the superconducting properties of the YBCO nanogaps, we bridge them with a thin Au film to realize a proximity-based  $S$ - $N$ - $S$  Josephson junction. The devices fabricated by using this approach have a proximity coupling up to 85 K. Figure 7(b) shows an example of the IVC at 73 K. The curve can be well described by the resistively shunted junction model in the presence of thermal noise [51]. The dependence of the Josephson critical current as a function of the external magnetic field, applied in the plane of the junction, is shown in Fig. 7(c). The magnetic field pattern of the critical current is close to Fraunhofer-like with a modulation period  $\Delta B \sim 1 \text{ mT}$  [see Fig. 7(c)]. This value is in reasonable agreement with the predicted period [52]  $\Delta B \sim 1.84\Phi_0/w_J^2$  for thin-film planar junctions with

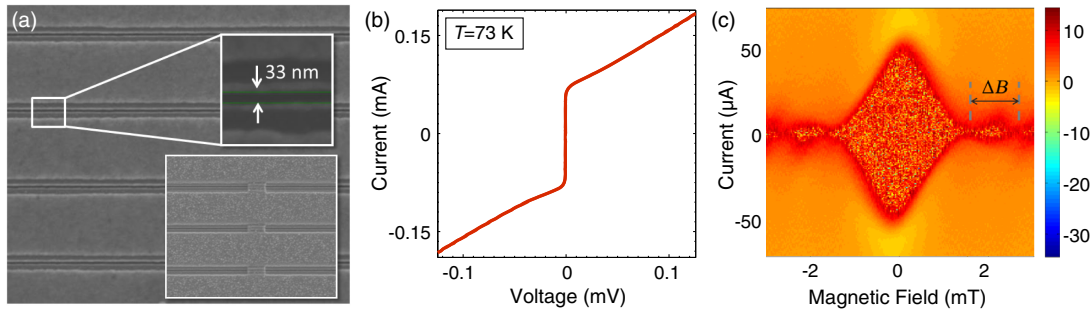


FIG. 7. (a) SEM image of an encapsulated YBCO nanogap with a Pt/Au bilayer. In the bottom right inset, the encapsulated YBCO nanogaps are bridged with a thin Au bar. (b) IV curves of a YBCO-Au-YBCO junction, with  $w_J = 3 \mu\text{m}$ , at 73 K. (c) Logarithmic differential conductance ( $dV/dI$ ) as a function of the current bias and applied magnetic field for the YBCO-Au-YBCO junction at 73 K, presented in (b).

$w_J \sim 3 \mu\text{m}$  the width of the junction. The position of the first minimum, i.e., half the width of the main lobe, is larger than  $\Delta B$ . This can be understood from the fact that our junction is at the border of a short-to-long junction,  $w_J \gtrsim l_J$ , with  $l_J = (\Phi_0/4\pi\mu_0\lambda_L J_C) \sim 1 \mu\text{m}$  the Josephson penetration depth for thin-film junctions [53]. Indeed, in this limit for small field values, the junction is in the Meissner regime, where screening currents around the junction cause the critical current to decrease linearly with the applied field  $I_C(B) = I_C(0)(1 - |B|/B_C)$  with  $B_C > \Delta B$  [54,55].

The junction resistance is also nearly temperature independent, and for the sample of Fig. 7(b) it has a value  $R_N$  of  $1.5 \Omega$ . We characterize the transport properties of microbridges of Au of the same thickness used to encapsulate the electrodes and to bridge the nanogap. The resistivity of the Au bars is of the order of  $1 \times 10^{-8} \Omega\text{m}$  at 4.2 K, which gives a value for the resistance of the Au channel of about  $7.5 \text{ m}\Omega$ , much lower than the resistance  $R_N$  of the junction. Therefore, we conclude that the value of  $R_N$  is mostly due to the contact resistance YBCO/Au. Moreover, the rather high values for the critical current density  $J_C$  we get at 77 K,  $J_C(77 \text{ K}) \sim (2-4) \times 10^4 \text{ A/cm}^2$ , and at 4.2 K,  $J_C(4.2 \text{ K}) \sim (1-2) \times 10^6 \text{ A/cm}^2$ , are due to the low value achieved for the YBCO/Au contact resistance  $R_C$ .

## VI. SUMMARY AND CONCLUSIONS

In conclusion, we perform a systematic study on YBCO nanowires, having different widths (60–700 nm) and lengths (1–10  $\mu\text{m}$ ). The wires, realized through three *e*-beam lithographic steps, are protected by means of a Pt/Au bilayer, covering their sides. After the nanopatterning, an *ex situ* ozone annealing is applied to the nanostructures, in order to recover the possible oxygen out-diffused during the fabrication. We characterize the nanowires by  $R(T)$  and *IVC* measurements, performed both before and after the ozonation. By comparing the superconducting properties of these nanowires with those of YBCO nanowires realized in a single *e*-beam lithography step and with those of YBCO nanowires realized by two *e*-beam steps (where the sides are not protected by Pt/Au), we conclude that the encapsulation is instrumental to achieve rather homogeneous nanostructures when several *e*-beam steps are required. We also show the fundamental role of the ozonation treatment, which for three lithographic step nanowires works to homogenize the nanostructures, healing regions where the superconductivity was previously depressed. The feasibility of our nanogaps to study the proximity-induced Josephson effect in *S-N-S* junctions is demonstrated by bridging the nanostructure with a thin Au film. We observe Josephson coupling up to 85 K with a Fraunhofer-like magnetic-field dependence. Moreover, conductance measurements on Au/YBCO interfaces also reveal that the heavily underdoped regions, close to the

metal-insulator transition, on the side of the nanogap, recover their original doping after ozonation. Our study clearly shows that these YBCO nanogaps can represent a platform for studying new physics in hybrid devices beyond the present state of the art.

## ACKNOWLEDGMENTS

This work is partially supported by the Swedish Research Council (VR) and by the Swedish Foundation for Strategic Research (SSF) under the project “Graphene based high-frequency electronics” and by the Knut and Alice Wallenberg Foundation under the project “Dirac Materials.” R. B. is supported by a grant from the Area of Advance Nano. Clean-room processing is achieved by using equipment sponsored by the Knut and Alice Wallenberg Foundation. The authors thank Professor Francesco Tafuri for useful discussions.

- 
- [1] A. C. Potter and L. Fu, Anomalous supercurrent from Majorana states in topological insulator Josephson junctions, *Phys. Rev. B* **88**, 121109 (2013).
  - [2] F. Tafuri, D. Massarotti, L. Galletti, D. Stornaiuolo, D. Montemurro, L. Longobardi, P. Lucignano, G. Rotoli, G. P. Pepe, A. Tagliacozzo, and F. Lombardi, Recent achievements on the physics of high- $T_c$  superconductor Josephson junctions: Background, perspectives and inspiration, *J. Supercond. Novel Magn.* **26**, 21 (2013).
  - [3] P. Zareapour, A. Hayat, S. Y. F. Zhao, M. Kreshchuk, Y. K. Lee, A. A. Reijnders, A. Jain, Z. Xu, T. S. Liu, G. D. Gu, S. Jia, R. J. Cava, and K. S. Burch, Evidence for a new excitation at the interface between a high- $T_c$  superconductor and a topological insulator, *Phys. Rev. B* **90**, 241106 (2014).
  - [4] J. Linder, Y. Tanaka, T. Yokoyama, A. Sudbø, and N. Nagaosa, Unconventional Superconductivity on a Topological Insulator, *Phys. Rev. Lett.* **104**, 067001 (2010).
  - [5] P. Lucignano, A. Mezzacapo, F. Tafuri, and A. Tagliacozzo, Advantages of using high-temperature cuprate superconductor heterostructures in the search for Majorana fermions, *Phys. Rev. B* **86**, 144513 (2012).
  - [6] Y. Kim, J. Cano, and C. Nayak, Majorana zero modes in semiconductor nanowires in contact with higher- $T_c$  superconductors, *Phys. Rev. B* **86**, 235429 (2012).
  - [7] S. Takei, B. Fregoso, V. Galitski, and S. Das Sarma, Topological superconductivity and majorana fermions in hybrid structures involving cuprate high- $T_c$  superconductors, *Phys. Rev. B* **87**, 014504 (2013).
  - [8] P. Lucignano, F. Tafuri, and A. Tagliacozzo, Topological rf SQUID with a frustrating  $\pi$  junction for probing the Majorana bound state, *Phys. Rev. B* **88**, 184512 (2013).
  - [9] C. Nayak, S. Simon, A. Stern, M. Freedman, and S. Das Sarma, Non-Abelian anyons and topological quantum computation, *Rev. Mod. Phys.* **80**, 1083 (2008).
  - [10] A. Stern, Non-Abelian states of matter, *Nature (London)* **464**, 187 (2010).

- [11] Y. Zhang, Y.-W. Tan, H. L. Stormer, and P. Kim, Experimental observation of the quantum Hall effect and Berry's phase in graphene, *Nature (London)* **438**, 201 (2005).
- [12] A. Tzalenchuk, S. Lara-Avila, A. Kalaboukhov, S. Paolillo, M. Syväjärvi, R. Yakimova, O. Kazakova, T. Janssen, V. Fal'Ko, and S. Kubatkin, Towards a quantum resistance standard based on epitaxial graphene, *Nat. Nanotechnol.* **5**, 186 (2010).
- [13] P. Rickhaus, M. Weiss, L. Marot, and C. Schönenberger, Quantum Hall effect in graphene with superconducting electrodes, *Nano Lett.* **12**, 1942 (2012).
- [14] A. A. Golubov, M. Yu. Kupriyanov, and E. Il'ichev, The current-phase relation in Josephson junctions, *Rev. Mod. Phys.* **76**, 411 (2004).
- [15] R. P. Robertazzi, A. W. Kleinsasser, R. B. Laibowitz, R. H. Koch, and K. G. Stawiasz, In situ Ag/YBa<sub>2</sub>Cu<sub>3</sub>O<sub>7</sub> contacts for superconductor/normal-metal/superconductor devices, *Phys. Rev. B* **46**, 8456 (1992).
- [16] C.-H. Chen, I. Jin, S. P. Pai, Z. W. Dong, C. J. Lobb, T. Venkatesan, K. Edinger, J. Orloff, and J. Mengailis, Fabrication of high-temperature superconducting Josephson junctions on substrates patterned by focused ion beam, *Appl. Phys. Lett.* **73**, 1730 (1998).
- [17] R. H. Ono, J. A. Beall, M. W. Cromar, T. E. Harvey, M. E. Johansson, C. D. Reintsema, and D. A. Rudman, High-T<sub>C</sub> superconductor-normal metal-superconductor Josephson microbridges with high-resistance normal metal links, *Appl. Phys. Lett.* **59**, 1126 (1991).
- [18] P. A. Rosenthal, E. N. Grossman, R. H. Ono, and L. R. Vale, High temperature superconductor-normal metal-superconductor Josephson junctions with high characteristic voltages, *Appl. Phys. Lett.* **63**, 1984 (1993).
- [19] M. Grove, R. Dittmann, M. Bode, M. Siegel, and A. I. Braginski, Current transport across YBa<sub>2</sub>Cu<sub>3</sub>O<sub>7</sub>-Au interfaces, *Appl. Phys. Lett.* **69**, 696 (1996).
- [20] M. Bode, M. Grove, M. Siegel, and A. I. Braginski, Superconductor-normal-superconductor step-edge junctions with Au barriers, *J. Appl. Phys.* **80**, 6378 (1996).
- [21] S. Morohashi, J. Wen, Y. Enomoto, and N. Koshizuka, Fabrication process and interfacial study of high-T<sub>C</sub> Josephson junctions fabricated using the focused ion beam technique, *Jpn. J. Appl. Phys.* **38**, 698 (1999).
- [22] H. Y. Zhai, Q. Y. Chen, X. W. Xu, M. Strikovsky, J. Miller, and W. K. Chu, Planar SNS Josephson junctions using FIB processing of c-oriented YBCO thin films, *Physica C (Amsterdam)* **341–348**, 1587 (2000).
- [23] M. G. Forrester, J. Talvacchio, J. R. Gavaler, M. Rooks, and J. Lindquist, Fabrication and characterization of YBa<sub>2</sub>Cu<sub>3</sub>O<sub>7</sub>/Au/YBa<sub>2</sub>Cu<sub>3</sub>O<sub>7</sub> Josephson junctions, *IEEE Trans. Magn.* **27**, 3098 (1991).
- [24] M. Arzeo, F. Lombardi, and T. Bauch, Microwave losses in MgO, LaAlO<sub>3</sub>, and (La<sub>0.3</sub>Sr<sub>0.7</sub>)(Al<sub>0.65</sub>Ta<sub>0.35</sub>)O<sub>3</sub> dielectrics at low power and in the millikelvin temperature range, *Appl. Phys. Lett.* **104**, 212601 (2014).
- [25] R. Baghdadi, R. Arpaia, T. Bauch, and F. Lombardi, Toward YBa<sub>2</sub>Cu<sub>3</sub>O<sub>7-δ</sub> nanoscale structures for hybrid devices, *IEEE Trans. Appl. Supercond.* **25**, 1 (2015).
- [26] R. Arpaia, S. Nawaz, F. Lombardi, and T. Bauch, Improved nanopatterning for YBCO nanowires approaching the depairing current, *IEEE Trans. Appl. Supercond.* **23**, 1101505 (2013).
- [27] D. Gustafsson, D. Golubev, M. Fogelström, T. Claeson, S. Kubatkin, T. Bauch, and F. Lombardi, Fully gapped superconductivity in a nanometre-size YBa<sub>2</sub>Cu<sub>3</sub>O<sub>7-δ</sub> island enhanced by a magnetic field, *Nat. Nanotechnol.* **8**, 25 (2013).
- [28] S. Nawaz, R. Arpaia, F. Lombardi, and T. Bauch, Microwave Response of Superconducting YBa<sub>2</sub>Cu<sub>3</sub>O<sub>7-δ</sub> Nanowire Bridges Sustaining the Critical Depairing Current: Evidence of Josephson-like Behavior, *Phys. Rev. Lett.* **110**, 167004 (2013).
- [29] S. Nawaz, R. Arpaia, T. Bauch, and F. Lombardi, Approaching the theoretical depairing current in YBa<sub>2</sub>Cu<sub>3</sub>O<sub>7-x</sub> nanowires, *Physica C (Amsterdam)* **495**, 33 (2013).
- [30] See Supplemental Material at <http://link.aps.org/supplemental/10.1103/PhysRevApplied.4.014022> for more details about the fabrication of 1EBL, 2EBL, and 3EBL devices.
- [31] G. Papari, F. Carillo, D. Stornaiuolo, L. Longobardi, F. Beltram, and F. Tafuri, High critical current density and scaling of phase-slip processes in YBaCuO nanowires, *Supercond. Sci. Technol.* **25**, 035011 (2012).
- [32] R. Arpaia, M. Ejrnaes, L. Parlato, R. Cristiano, M. Arzeo, T. Bauch, S. Nawaz, F. Tafuri, G. P. Pepe, and F. Lombardi, Highly homogeneous YBCO/LSMO nanowires for photo-response experiments, *Supercond. Sci. Technol.* **27**, 044027 (2014).
- [33] N. E. Litombe, A. T. Bollinger, J. E. Hoffman, and I. Bozovic, La<sub>2-x</sub>Sr<sub>x</sub>CuO<sub>4</sub> superconductor nanowire devices, *Physica C (Amsterdam)* **506**, 169 (2014).
- [34] S. Abay, H. Nilsson, F. Wu, H. Xu, C. Wilson, and P. Delsing, High critical-current superconductor-InAs nanowire-superconductor junctions, *Nano Lett.* **12**, 5622 (2012).
- [35] H. Bartolf, A. Engel, A. Schilling, K. Il'in, M. Siegel, H.-W. Hübers, and A. Semenov, Current-assisted thermally activated flux liberation in ultrathin nanopatterned NbN superconducting meander structures, *Phys. Rev. B* **81**, 024502 (2010).
- [36] L. N. Bulaevskii, M. J. Graf, C. D. Batista, and V. G. Kogan, Vortex-induced dissipation in narrow current-biased thin-film superconducting strips, *Phys. Rev. B* **83**, 144526 (2011).
- [37] R. Arpaia, D. Golubev, R. Baghdadi, M. Arzeo, G. Kunakova, S. Charpentier, S. Nawaz, F. Lombardi, and T. Bauch, Resistive state triggered by vortex entry in YBa<sub>2</sub>Cu<sub>3</sub>O<sub>7-δ</sub> nanostructures, *Physica C (Amsterdam)* **506**, 165 (2014).
- [38] G. Papari, F. Carillo, D. Stornaiuolo, D. Massarotti, L. Longobardi, F. Beltram, and F. Tafuri, Dynamics of vortex matter in YBCO sub-micron bridges, *Physica C (Amsterdam)* **506**, 188 (2014).
- [39] R. Arpaia, S. Charpentier, R. Toskovic, T. Bauch, and F. Lombardi, YBa<sub>2</sub>Cu<sub>3</sub>O<sub>7-δ</sub> nanorings to probe fluxoid quantization in high critical temperature superconductors, *Physica C (Amsterdam)* **506**, 184 (2014).
- [40] J. Johansson, K. Cedergren, T. Bauch, and F. Lombardi, Properties of inductance and magnetic penetration depth in (103)-oriented YBa<sub>2</sub>Cu<sub>3</sub>O<sub>7-δ</sub> thin films, *Phys. Rev. B* **79**, 214513 (2009).

- [41] R. Arpaia, M. Arzeo, S. Nawaz, S. Charpentier, F. Lombardi, and T. Bauch, Ultra low noise  $\text{YBa}_2\text{Cu}_3\text{O}_{7-\delta}$  nano superconducting quantum interference devices implementing nanowires, *Appl. Phys. Lett.* **104**, 072603 (2014).
- [42] M. Tinkham, *Introduction to Superconductivity*, 2nd ed. (McGraw-Hill, New York, 1996).
- [43] A. Sawa, S. Kosaka, H. Obara, and K. Aoki, Low-pressure oxidation of  $\text{YBa}_2\text{Cu}_3\text{O}_{7-x}$  thin films in purified ozone, *IEEE Trans. Appl. Supercond.* **3**, 1088 (1993).
- [44] F. Herbstritt, T. Kemen, A. Marx, and R. Gross, Ultraviolet light assisted oxygenation process for submicron  $\text{YBa}_2\text{Cu}_3\text{O}_{7-\delta}$  thin film devices, *J. Appl. Phys.* **91**, 5411 (2002).
- [45] The reason for this discrepancy is given by the use at low temperatures of the Ginzburg-Landau theory, which instead is strictly valid only close to the superconducting transition. The calculations for the depairing critical current density in the clean and dirty limit at  $T = 0$  K predict a deviation from the Ginzburg-Landau limit by a maximum factor of 1.5 [46,47], which reconciles with the higher values of the critical current density extracted on our nanowires after the ozonation.
- [46] J. Bardeen, Critical fields and currents in superconductors, *Rev. Mod. Phys.* **34**, 667 (1962).
- [47] J.R. Clem and V.G. Kogan, Kinetic impedance and depairing in thin and narrow superconducting films, *Phys. Rev. B* **86**, 174521 (2012).
- [48] S.J. Rothman, J.L. Routbort, U. Welp, and J.E. Baker, Anisotropy of oxygen tracer diffusion in single-crystal  $\text{YBa}_2\text{Cu}_3\text{O}_{7-\delta}$ , *Phys. Rev. B* **44**, 2326 (1991).
- [49] W.L. McMillan and J. Mochel, Electron Tunneling Experiments on Amorphous  $\text{Ge}_{1-x}\text{Au}_x$ , *Phys. Rev. Lett.* **46**, 556 (1981).
- [50] H. Dreuth and H. Dederichs, Evaluation of low resistance contacts on  $\text{YBa}_2\text{Cu}_3\text{O}_7$  thin films using the transmission line model, *Supercond. Sci. Technol.* **6**, 464 (1993).
- [51] A. Barone and G. Paterno, *Physics and Applications of the Josephson Effect*, Vol. 1 (Wiley, New York, 1982).
- [52] P.A. Rosenthal, M.R. Beasley, K. Char, M.S. Colclough, and G. Zaharchuk, Flux focusing effects in planar thin-film grain-boundary Josephson junctions, *Appl. Phys. Lett.* **59**, 3482 (1991).
- [53] V.G. Kogan, V.V. Dobrovitski, J.R. Clem, Y. Mawatari, and R.G. Mints, Josephson junction in a thin film, *Phys. Rev. B* **63**, 144501 (2001).
- [54] C.S. Owen and D.J. Scalapino, Vortex structure and critical currents in Josephson junctions, *Phys. Rev.* **164**, 538 (1967).
- [55] A. Barone, W.J. Johnson, and R. Vaglio, Current flow in large Josephson junctions, *J. Appl. Phys.* **46**, 3628 (1975).